Supporting Materials – Supplements to:

Cosmic pears from the Havelland (Germany): Ribbeck, the twelfth recorded aubrite fall in history

by:

Addi Bischoff, Markus Patzek, Jean-Alix Barrat, Jasper Berndt, Henner Busemann, Detlev Degering, Tommaso Di Rocco, Jose R. A. Godinho, Dennis Harries, Dieter Heinlein, Armin Kriele, Daniela Krietsch, Colin Maden, Oscar Marchhart, Rachael M. Marshal, Martin Martschini, Silke Merchel, Andreas Möller, Andreas Pack, Herbert Raab, Maximilian P. Reitze, Ina Rendtel, Miriam Rüfenacht, Oliver Sachs, Maria Schönbächler, Anja Schuppisser, Iris Weber, Alexander Wieser, and Karl Wimmer.

The supplements contain the following items:

Supplement S1:

The Poem of Theodor Fontane

Herr von Ribbeck auf Ribbeck im Havelland

Herr von Ribbeck auf Ribbeck im Havelland,
Ein Birnbaum in seinem Garten stand,
Und kam die goldene Herbsteszeit

Und die Birnen leuchteten weit und breit,
Da stopfte, wenn's Mittag vom Turme scholl,
Der von Ribbeck sich beide Taschen voll,
Und kam in Pantinen ein Junge daher,
So rief er: »Junge, wiste 'ne Beer?«
Und kam ein Mädel, so rief er: »Lütt Dirn,
Kumm man röwer, ick hebb 'ne Birn.«

So ging es viel Jahre, bis lobesam
Der von Ribbeck auf Ribbeck zu sterben kam.

Er fühlte sein Ende. 's war Herbsteszeit,
Wieder lachten die Birnen weit und breit;
Da sagte von Ribbeck: »Ich scheide nun ab.
Legt mir eine Birne mit ins Grab.«
Und drei Tage drauf, aus dem Doppeldachhaus,
Trugen von Ribbeck sie hinaus,
Alle Bauern und Büdner mit Feiergesicht
Sangen »Jesus meine Zuversicht«,
Und die Kinder klagten, das Herze schwer:
»He is dod nu. Wer giwt uns nu 'ne Beer?«

So klagten die Kinder. Das war nicht recht -
Ach, sie kannten den alten Ribbeck schlecht;
Der neue freilich, der knausert und spart,
Hält Park und Birnbaum strenge verwahrt.
Aber der alte, vorahnend schon
Und voll Mißtraun gegen den eigenen Sohn,
Der wußte genau, was damals er tat,
Als um eine Birn' ins Grab er bat,
Und im dritten Jahr aus dem stillen Haus
Ein Birnbaumsprößling sproßt heraus.

Und die Jahre gingen wohl auf und ab,
Längst wölbt sich ein Birnbaum über dem Grab,
Und in der goldenen Herbsteszeit
Leuchtet's wieder weit und breit.
Und kommt ein Jung' übern Kirchhof her,
So flüstert's im Baume: »Wiste 'ne Beer?«
Und kommt ein Mädel, so flüstert's: »Lütt Dirn,
Kumm man röwer, ick gew' di 'ne Birn.«

So spendet Segen noch immer die Hand
Des von Ribbeck auf Ribbeck im Havelland.

https://www.vonribbeck.de/gedicht-herr-von-ribbeck-auf-ribbeck-im-havelland/

Squire von Ribbeck at Ribbeck in Havelland

Squire von Ribbeck at Ribbeck in Havelland,
In his garden there stood a pear tree grand,
And when autumn came round, the golden tide,

And pears were glowing far and wide,
Squire von Ribbeck, when noon rang out, would first
Fill both his pockets full to burst.
And then, when a boy in his clogs came there,
He called: "My lad, do you want a pear?"
He would hail a girl that chanced to pass:
"Come over, I have a pear, little lass!"

Many years thus went, till the noble and high
Squire von Ribbeck at Ribbeck came to die.
He felt his end. It was autumntide.
Again pears were smiling far and wide.
"I depart now this life" von Ribbeck said.
I wish that a pear in my grave be laid".
And after three days, from this mansard roofed hall,
Squire von Ribbeck was carried out, `neath a pall.
All farmers and cottagers, solemm-faced,
Sang: "Jesus, in Thee my trust is placed",
And the children lamented, with hearts like lead:
"Who`ll give us a pear, now that he is dead.?"
So the children lamented. It was unkind,

As they did not know old Ribbeck´s mind.
True, the new one is skimping niggardly,
Keeps park and pears tree `neath lock and key;
But having forebodings, the older one,
And full of distrust for his proper son,
Knew well what he did, when the order he gave,
That a pear should be laid in his grave.

From the silent dwelling, after three years,
The tip of a pear tree seedling appears.
And year after year, the seasons go round,
Long since a pear tree is shading the mound.

And in the golden autumntide
Again it is glowing far and wide.
When a boy is crossing the churchyard there,
The tree is whispering: Want a pear?"
And when a girl chances to pass,
It whispers: "Come here for a pear, little lass."

Thus blessings still dispensses the hand
Of von Ribbeck at Ribbeck in Havelland.

https://www.vonribbeck.de/ribbeck-international/

Song by Achim Reichel (Live in Hamburg, 2003):
YouTube: https://m.youtube.com/watch?v=LqNY3PeiUn0

Supplement - Table S1

Table S1: Samples recovered by the *Arbeitskreis Meteore* (AKM numbers), by the *Museum für Naturkunde* (MFN numbers) and by other institutions and private searchers (F numbers). The first recovery was reported January 25 at 11:48 h (Sample F14). TKW = total known weight. The recoveries of 202 registered samples have been reported to our group by June 29, 2024.

Sample No.	Date (MEZ)	Coordinates N, E	Mass (g)	Comments
AKM01	1/27/2024 9:22	52.618824, 12.765795	45.89	Many fragments (>10) within an area of ~5 m^2
	3 largest pieces	AKM01A	14.76	
		AKM01B	19.55	Used for gamma-spectroscopy; Figs. 2 and S1
		AKM01C	4.30	Sample for mineralogical investigations; Fig. 2
AKM02	1/27/2024 11:09	52.618272, 12.764892	20.51	
AKM03	1/27/2024 14:04	52.615064, 12.772622	15.59	Shattered on the ground. 12 larger fragments
AKM04	1/28/2024 13:15	52.609979, 12.796870	4.77	
AKM05	1/28/2024 16:16	52.617626, 12.769955	25.48	Used for gamma-spectroscopy
AKM06	2/3/2024 13:50	52.612833, 12.807528	2.86	Oriented sample
AKM07	2/4/2024 10:51	52.612117, 12.803961	3.73	2 samples, largest sample: 3.65g
AKM08	3/9/2024 16:46	52.608960, 12.808661	7.36	Distinct foamy fusion crust on one side
MFN01		52.610000, 12.779722	8.10	
MFN02		52.610000, 12.779444	4.70	
MFN03		52.611933, 12.781500	12.80	
MFN04		52.612500, 12.778333	24.10	
MFN05		52.609722, 12.803611	3.24	
MFN06		52.608333, 12.799167	8.30	
MFN07		unknown	3.40	
MFN08		52.609722, 12.796944	4.40	
MFN09		52.610250, 12.797267	8.10	
MFN10		52.610000, 12.792222	2.80	
MFN11		52.617222, 12.765278	19.00	
MFN12		52.615556, 12.775556	8.70	
MFN13		52.615556, 12.775556	8.80	Same location as MFN12?
MFN14		52.611667, 12.803056	3.10	
MFN15		52.611667, 12.800278	9.00	
MFN16		52.610556, 12.805278	2.00	
MFN17		52.610278, 12.805278	4.20	
MFN18		52.61137, 12.80075	2.80	
MFN19		52.61164, 12.79534	2.80	
MFN20		52.608611, 12.808056	6.10	
MFN21		52.611944, 12.805000	3.20	
MFN22		52.610833, 12.806667	3.70	
MFN23		52.608917, 12.821444	3.65	
MFN24		52.609667, 12.820306	1.76	
MFN25		52.61165, 12.79531	1.56	

F01	1/26/2024 9:36	52.622939, 12.739409	111.19	Mass loss after drying
F02	1/26/2024	52.615386, 12.763814	37.79	
F03	2/3/2024 16:42	52.603997, 12.811897	5.23	Fits to F33
F04	2/17/2024	52.603889, 12.833333	1.10	
F05	1/27/2024 12:45	52.616565, 12.772460	21.08	Used for density analysis; Fig. S1
F06	1/27/2024	52.618136, 12.759248	14.15	Used for density analysis; Fig. S1
F07	1/27/2024 13:05	52.615488, 12.773502	10.11	Used for density analysis; Fig. 1 and S3
F08	1/28/2024	52.615389, 12.774861	5.20	
F09	1/29/2024 15:36	52.619717, 12.758600	3.95	
F10	2/10/2024	52.623917, 12.758783	24.37	
F11	1/28/2024	unknown	6.60	
F12		52.613147, 12.792849	5.00	Mass estimated, exact find location unknown
F13	1/29/2024	52.623794, 12.739908	212.00	Largest mass. Wet: 225 g
F14	1/25/2024 11:48	52.627236, 12.730710	171.66	First recovery; 3 fragments
F15	1/27/2024	52.619111, 12.754576	53.90	
F16	1/26/2024	52.613975, 12.761197	28.00	
F17	2/1/2024 15:52	52.612885, 12.796214	2.21	
F18	2/2/2024	52.610010, 12.798060	3.40	
F19	1/28/2024	52.620850, 12.761133	9.80	
F20	1/28/2024	52.611617, 12.777733	3.40	
F21	1/26/2024 14:50	52.625694, 12.745028	52.56	
F22	2/4/2024	52.615269, 12.781858	5.19	
F23	1/30/2024 10:09	52.609530, 12.789356	11.04	
F24	1/30/2024 10:05	52.6124, 12.7620	14.84	
F25	1/30/2024 11:01	52.608439, 12.789238	21.00	
F26	2/1/2024	52.612778, 12.778333	9.60	
F27		52.610454, 12.796985	2.64	
F28		52.610348, 12.797784	5.30	
F29	1/27/2024 14:23	52.617995, 12.759026	16.00	
F30	2/2/2024 10:43	52.607806, 12.796111	9.20	
F31	2/2/2024 13:36	52.606389, 12.806500	8.00	
F32	2/3/2024 10:08	52.606889, 12.804694	5.70	
F33	2/3/2024 9:03	52.608611, 12.803889	4.93	Fits to F03.
F34	2/3/2024	52.610467, 12.808550	4.14	
F35		52.611409, 12.803484	5.52	
F36		52.610563, 12.802453	3.20	
F37	2/10/2024	52.610814, 12.799791	4.64	Oriented specimen, distinct fusion crust
F38	2/3/2024	52.61167, 12.78416	12.40	
F39	2/4/2024	52.615000, 12.792500	8.30	
F40	2/4/2024	52.613111, 12.788083	6.94	Extremely oriented specimen
F41	1/30/2024 1:29	52.613667, 12.788694	14.13	
F42	2/4/2024 1:09	52.613250, 12.793750	2.82	

F43	2/4/2024 11:25	52.611306, 12.802611	12.40	
F44	1/29/2024 15:58	52.613306, 12.792694	3.85	
F45	2/3/2024 11:22	52.623541, 12.745518	22.04	
F46	1/27/2024 9:34	52.620568, 12.755650	21.16	
F47	2/7/2024	52.608834, 12.799883	6.00	
F48	2/8/2024	52.615613, 12.765852	10.30	
F49	2/6/2024	52.611340, 12.788779	7.90	
F50	2/9/2024	unknown	4.30	
F51		52.609382, 12.786924	16.34	
F52		52.609530, 12.789356	2.10	
F53		52.611018, 12.789700	5.10	
F54		52.610796, 12.790438	4.10	
F55	2/3/2024 10:44	52.613500, 12.783500	11.11	
F56	2/12/2024	52.605778, 12.830713	1.70	
F57	2/13/2024	52.605826, 12.830215	2.80	
F58	2/14/2024	52.605834, 12.828865	1.50	
F59	2/14/2024	52.605997, 12.828816	5.10	
F60	2/14/2024	52.604359, 12.830971	1.55	
F61	2/17/2024	52.605556, 12.835833	1.00	
F62	3/5/2024	52.607729, 12.836088	2.00	Mass estimated
F63	2/2/2024	unknown	3.28	
F64	2/10/2024 11:17	52.608380, 12.818980	2.03	
F65	2/3/2024	unknown	3.30	
F66	2/4/2024 16:16	52.611788, 12.790319	1.70	
F67	2/9/2024	unknown	10.00	
F68	2/9/2024	unknown	4.30	White fusion crust dominating
F69	2/10/2024	52.603500, 12.819300	1.96	"Dalmatian stone"; Figs. S2 and S3; dry: 1.94 g
F70	2/11/2024	52.607750, 12.817778	2.90	
F71	2/11/2024	52.606111, 12.820472	2.09	
F72	2/3/2024	52.608095, 12.817194	2.21	
F73	2/5/2024	52.612729, 12.790482	3.45	
F74	2/5/2024	52.612684, 12.790166	9.80	
F75	2/7/2024	52.607820, 12.808827	2.74	
F76	2/7/2024	52.605820, 12.817607	7.88	
F77	2/8/2024	52.605995, 12.826289	2.92	
F78	2/8/2024	52.606953, 12.826618	1.49	
F79	2/8/2024	52.605350, 12.826779	1.95	
F80	2/9/2024	52.605815, 12.827032	1.87	
F81	2/9/2024	52.606078, 12.822707	3.27	
F82	2/9/2024	52.605046, 12.835372	1.41	Spectacular fusion crust; Figs. 1 and S3
F83	2/11/2024	52.606797, 12.830728	5.41	
F84	2/12/2024	52.605277, 12.831881	2.77	
F85	2/11/2024 13:00	52.606528, 12.819250	2.00	

F86	2/11/2024	52.605611, 12.818028	4.22	
F87	2/11/2024	52.606167, 12.828389	1.56	
F88	2/11/2024	52.605861, 12.821639	2.60	Many fragments
F89	2/3/2024	52.613000, 12.795000	12.00	
F90	3/7/2024	unknown	unknown	
F91	2/11/2024	52.616250, 12.751389	47.50	
F92	2/12/2024	52.608376, 12.818824	1.61	
F93	2/12/2024	52.608514, 12.817411	1.57	
F94	2/14/2024	52.616557, 12.775251	12.32	
F95	2/15/2024 15:30	52.608102, 12.804762	7.79	
F96	2/15/2024	52.6061, 12.8254	2.69	
F97	2/12/2024	52.60927, 12.79625	3.86	
F98	2/15/2024 15:51	52.604167, 12.815556	3.70	
F99	2/15/2024 17:13	52.603333, 12.819444	4.20	
F100	2/14/2024	52.610283, 12.802017	3.00	
F101	2/16/2024	52.606536, 12.823450	2.17	
F102	2/11/2024	52.605617, 12.829624	2.67	
F103	2/12/2024	52.605694, 12.831869	2.15	
F104	2/18/2024 11:46	52.604917, 12.828194	1.38	
F105	2/18/2024 15:25	52.605361, 12.824361	2.47	Many fragments
F106	2/3/2024	52.605361, 12.807833	5.45	
F107	2/4/2024 10:15	52.610639, 12.798917	2.57	
F108	2/4/2024 15:07	52.614056, 12.790222	4.99	
F109	2/9/2024 10:59	52.612972, 12.795500	9.52	
F110	2/9/2024 14:05	52.613194, 12.799361	4.96	
F111	2/21/2024 15:00	52.606303, 12.822091	2.40	
F112	2/3/2024	52.605610, 12.814440	5.30	
F113	2/15/2024	52.610447, 12.802425	1.89	
F114	2/17/2024	52.609533, 12.801917	2.53	
F115	2/15/2024	52.608794, 12.802175	3.38	
F116	2/15/2024	52.609767, 12.803567	6.72	
F117	2/16/2024	52.608583, 12.804517	9.27	
F118	2/22/2024	52.607579, 12.823430	2.38	
F119	2/27/2024	52.604900, 12.822900	1.07	
F120	2/25/2024	52.607633, 12.801567	2.86	
F121		52.609846, 12.803262	5.30	
F122		52.609686, 12.803321	4.20	
F123		52.613056, 12.769722	6.10	
F124	1/31/2024 9:54	52.609347, 12.810156	2.30	Meteorite broke during recovery
F125	1/31/2024 16:17	52.608403, 12.805183	7.00	
F126	2/9/2024 9:23	52.608322, 12.828047	2.55	
F127	2/9/2024 9:46	52.609700, 12.828056	3.06	
F128	2/9/2024 14:42	52.609436, 12.827539	2.30	

F129	2/10/2024 11:33	52.607147, 12.827031	2.79	
F130	2/10/2024 13:13	52.607431, 12.826897	2.19	Shattered on the ground
F131	2/10/2024 14:06	52.604900, 12.826814	0.80	
F132	2/11/2024 14:53	52.606936, 12.832972	1.84	
F133	2/12/2024 16:09	52.606975, 12.835956	1.33	
F134	2/13/2024 12:13	52.604939, 12.838328	1.81	
F135	1/17/2024 17:08	52.608106, 12.837758	1.83	
F136	1/17/2024 17:09	52.608106, 12.837758	1.90	One meter south of F135
F137	2/18/2024 15:24	52.605536, 12.835353	3.80	
F138	2/23/2024 10:50	52.604564, 12.833386	2.10	
F139	2/24/2024 10:45	52.604528, 12.833889	1.62	
F140	2/22/2024 13:13	52.604694, 12.815111	2.25	
F141	2/22/2024 14:13	52.602833, 12.813806	2.67	
F142	2/22/2024 16:44	52.603972, 12.812000	4.45	
F143	2/28/2024 15:00	52.613083, 12.801583	3.17	
F144	2/29/2024 10:25	52.603111, 12.824167	1.32	
F145	3/2/2024	unknown	5.00	Mass estimated
F146	3/3/2024 10:14	52.606000, 12.839944	0.66	Many fragments
F147	3/2/2024 17:09	52.609090, 12.795220	1.56	Sample broke during recovery; largest: 0.434 g
F148	3/5/2024 16:18	52.604320, 12.829750	3.01	Broken piece (2.56 g, 0.22 g, + 0.23 g small grains)
F149	3/6/2024 15:36	52.608960, 12.784350	4.48	Large piece of 4.36 g and grains
F150	3/7/2024	unknown	unknown	
F151	3/7/2024	unknown	unknown	
F152		unknown	1.40	
F153	3/11/2024	52.606367, 12.823033	1.49	Oriented specimen; distinct foamy fusion crust
F154		52.60261, 12.81836	3.96	
F155		52.61242, 12.80292	2.27	
F156		52.60683, 12.80355	1.10	
F157		52.609378, 12.786906	unknown	Meteorite broke during recovery
F158	3/18/2024	52.605278, 12.811389	2.88	
F159	3/20/2024	52.608898 12.817243	0.87	Oriented specimen “Bullet” with white fusion crust
F160	3/3/2024	52.618750, 12.765133	17.60	Oriented specimen. Broke apart during drying
F161		52.609111, 12.825550	2.00	
F162		52.614819, 12.768983	4.00	
F163	3/17/2024	52.598434, 12.862494	2.23	Meteorite broke during recovery
F164		unknown	unknown	
F165	2/1/2024	52.606, 12.820	1.95	Location estimated
F166	2/2/2024	unknwon	unknown	
F167	2/3/2024	unknown	unknown	
F168	5/13/2024	unknown	3.83	
F169	3/27/2024 14:47	52.605389, 12.838528	3.34	Shattered into 5 fragments
202 pieces		**Sum (TKW)**	**1784.66**	

Supplement – Fig. S1

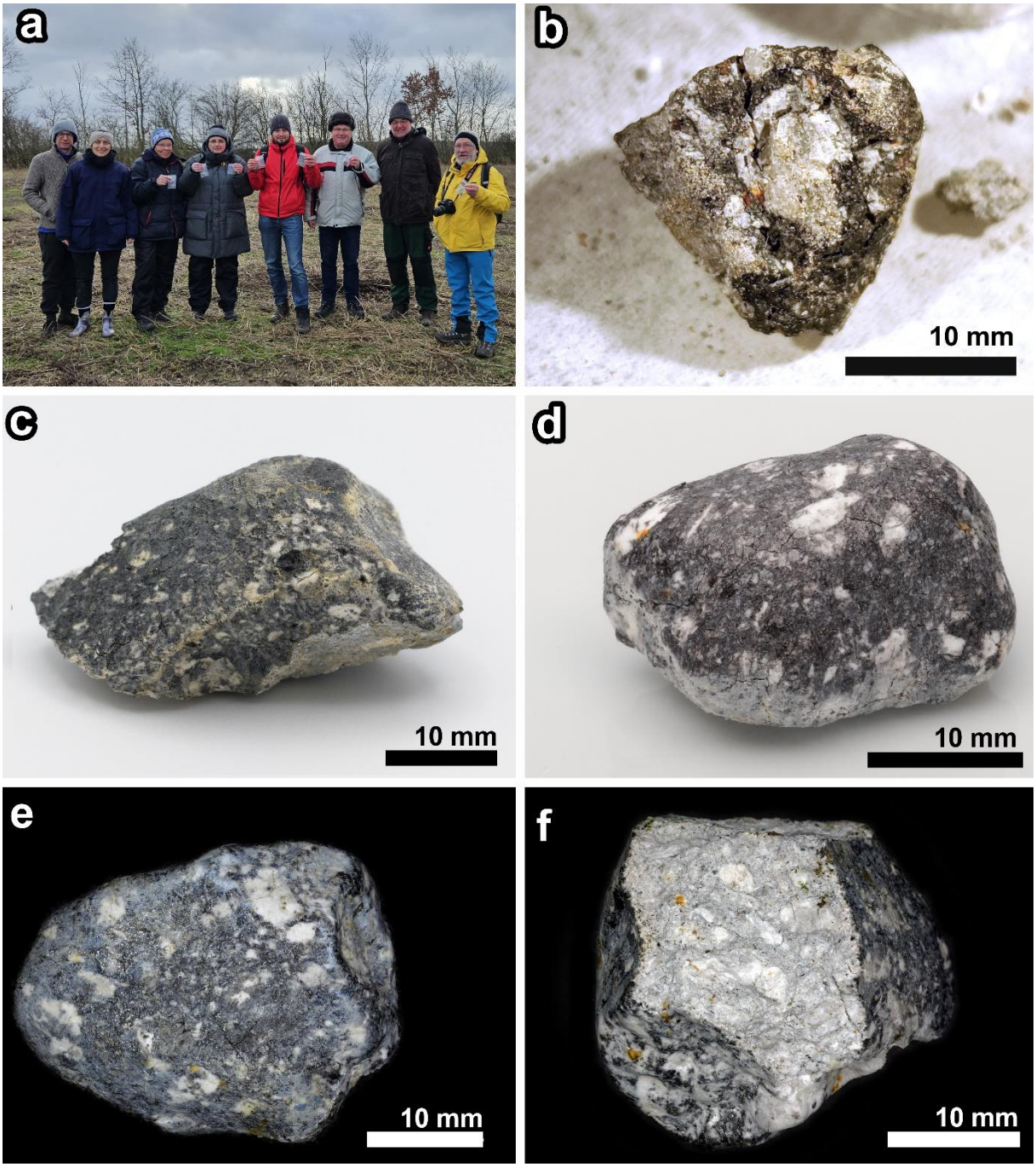

Fig. S1: (a) Search team of the *Arbeitskreis Meteore* (AKM) with some guests during the successful search January 27, 2024 (Photo: AKM). (b) The 4.3 g piece (fragment of AKM01; Table S1) studied in detail in this work found the same day. (c) 19.55 g fragment used for gamma spectroscopy also from AKM01 (Table S1; Photo: AKM). (d) Fragment F07 (Table S1) of about 10 g used for density measurements. (e) Fragment F05 of 21.08 g used for density measurements; Photo: O. Lenzen. (f) Sample F06 of 14.15 g also used for the determination of the density; Photo: O. Lenzen.

Supplement – Fig. S2

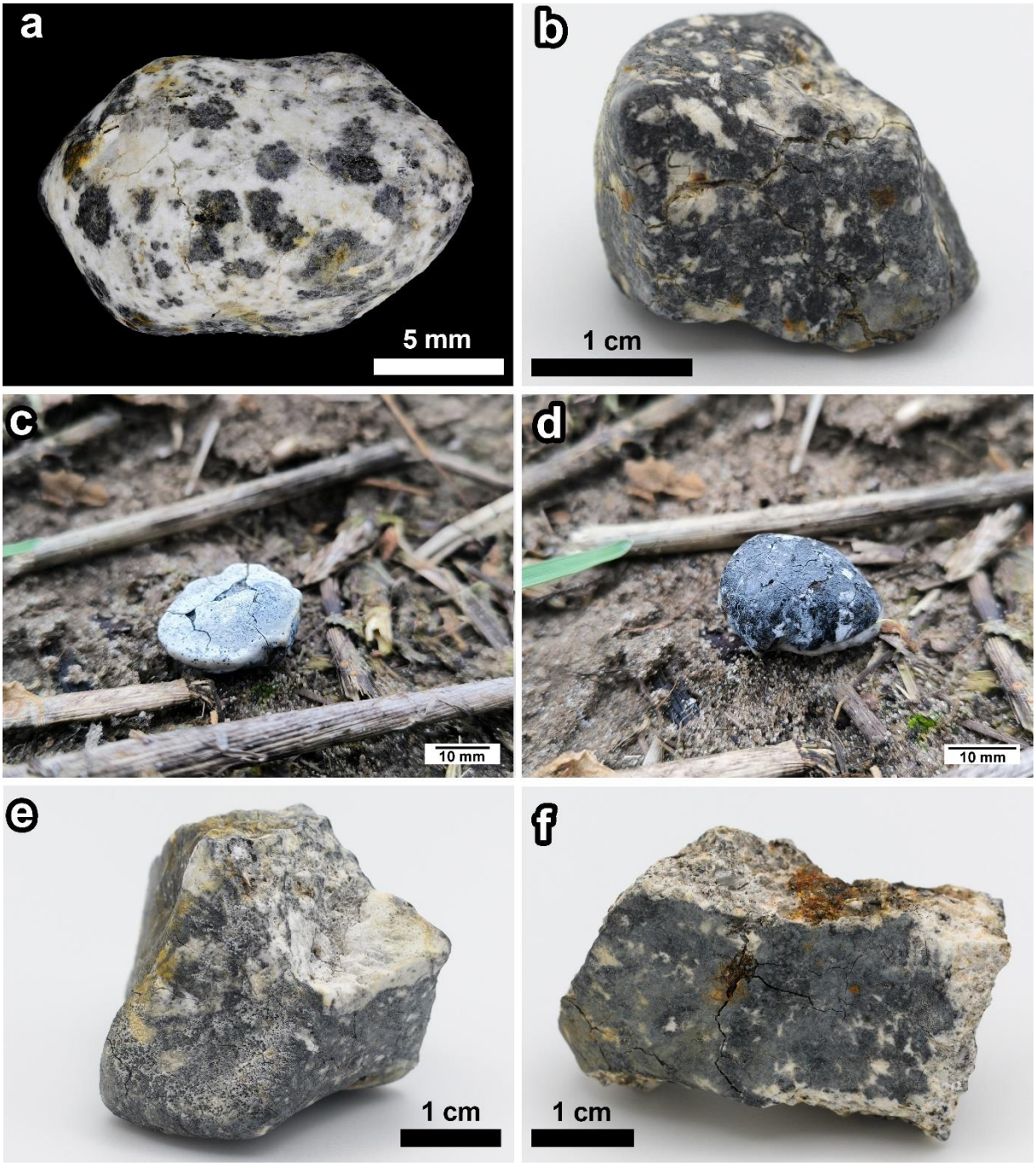

Fig. S2: Images of recovered fragments of Ribbeck: (a) Image of the complete "Dalmatian stone" F69 weighing 1.937 g (Photo: O. Lenzen). (b) Fragment AKM08 of 7.36 g (Photo: AKM). (c) and (d) show the 6.94 g flight-oriented sample F40 in situ (c) and turned over (d); (Photos: Julien Liehmann). (e) Fragment AKM05 of 25.48 g (Photo: AKM). (f) Stone AKM02 of 20.51 g, which clearly is a fragment of a once larger rock having experienced severe terrestrial weathering already one week after the fall. (Photo: AKM).

Supplement – Fig. S3

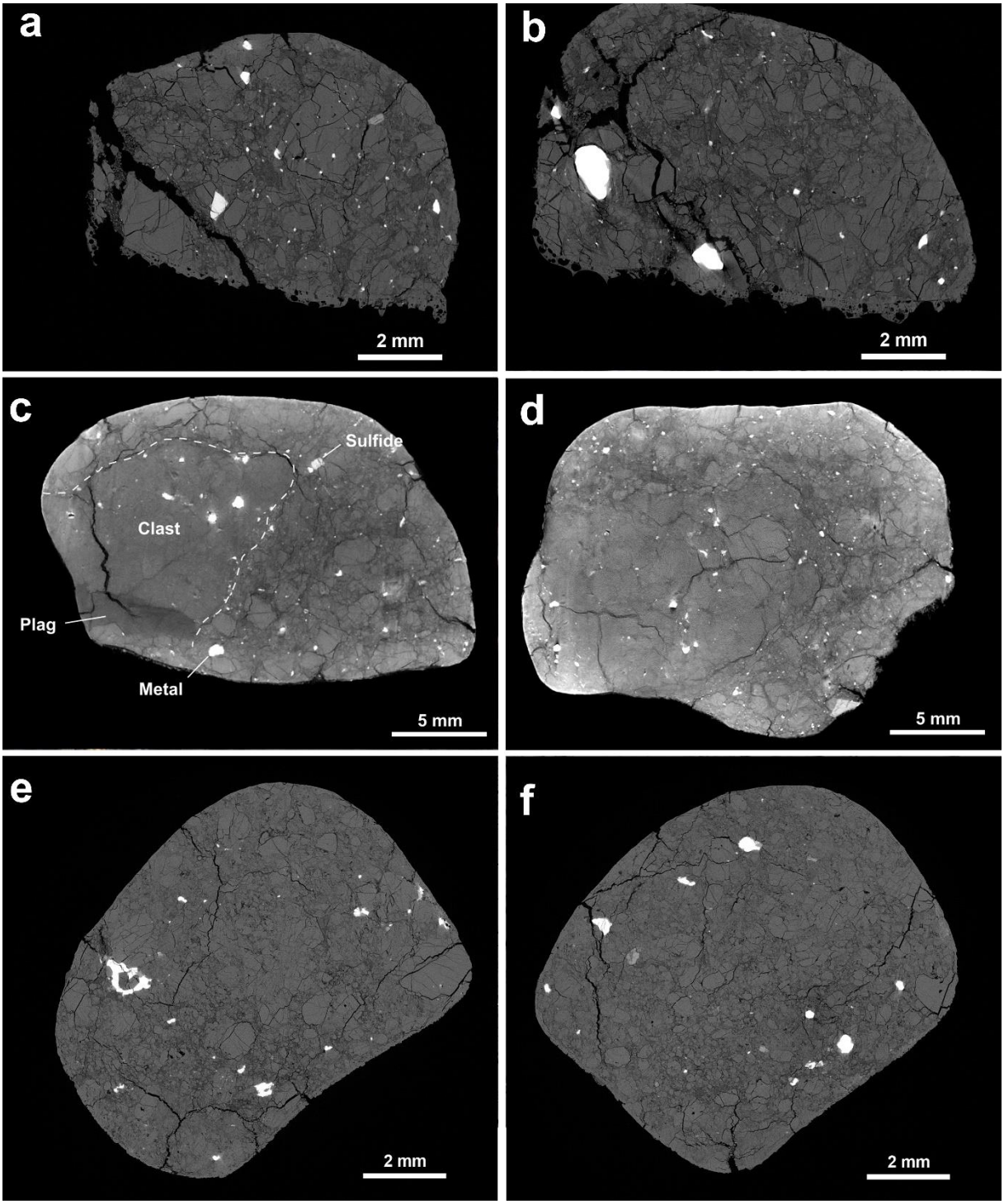

Fig. S3: (a) Computed tomography (CT) slice of Ribbeck sample F82 illustrating the brecciated interior of Ribbeck. (b) CT slice of Ribbeck sample F82 with a metal grain of 1.5 mm in length, which are rare in this size. (c) CT slice of Ribbeck sample F07 with a visible large coarse-grained clast (likely enstatite) that can be well distinguished from the brecciated rest of the sample. (d) CT slice of Ribbeck sample F07 with visible smaller metal and sulfide grains and a more coarse-grained area in the center. (e) CT slice of Ribbeck sample F69 showing a typical brecciation in the interior of this sample. (f) Slice of Ribbeck sample F69 illustrating the uneven distribution of metal grains within specimens of the Ribbeck fall.

Supplement – Fig. S4

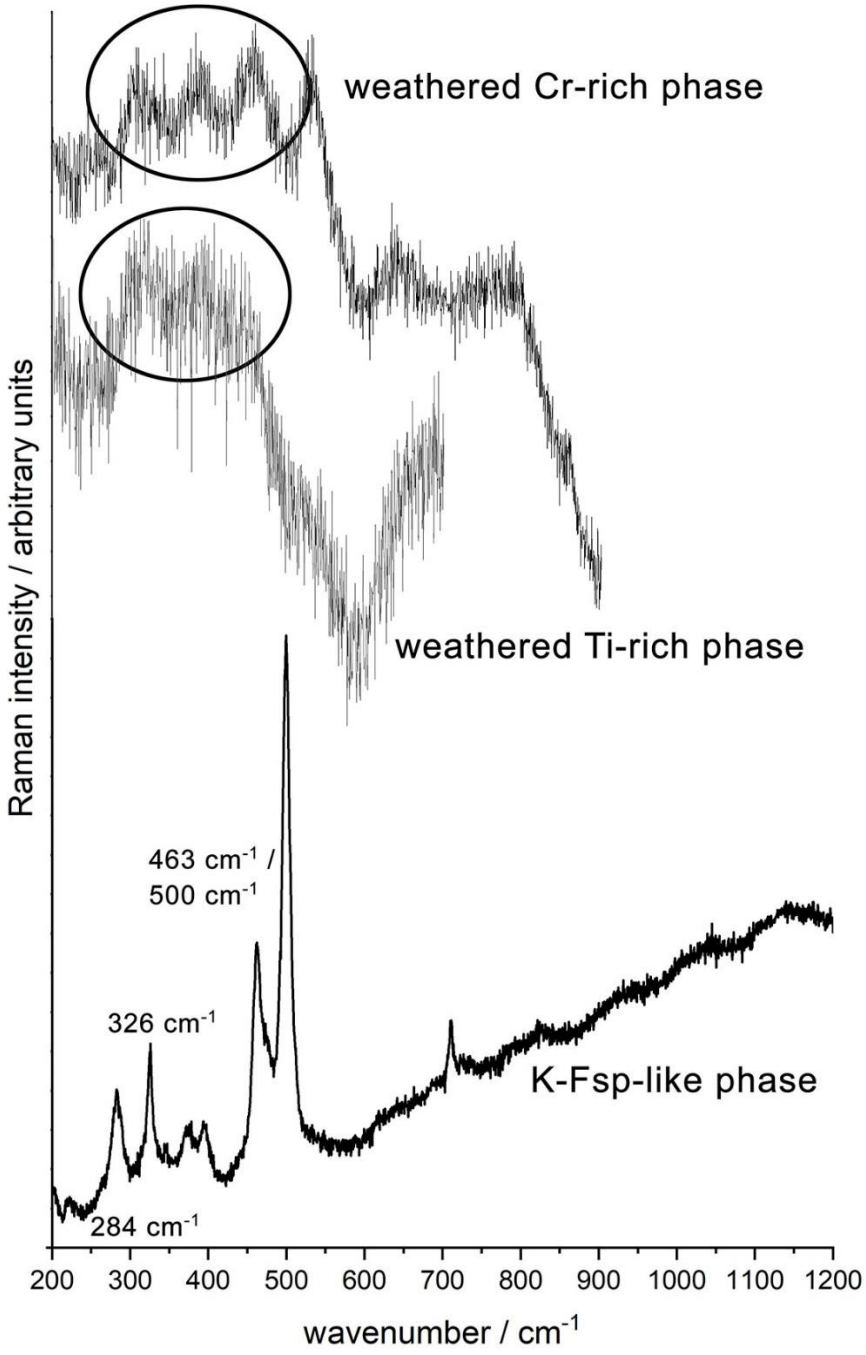

Fig. S4: Raman spectra of the unusual, ”altered” phases (see Tables 1 and 2). The S-bearing K-Fsp-like phase is plotted in the Raman range from 200 cm^{-1} to 1200 cm^{-1} and can be identified as a feldspar based on the typical Stoke shifts at 284 cm^{-1}, 326 cm^{-1}, and the double peak 463 cm^{-1} / 500 cm^{-1}. The “altered” sulfide phases are analyzed only from 200 cm^{-1} to 700 cm^{-1} and 900 cm^{-1}, respectively, due to their instability under the Ramen laser. Typical sulfide Stoke shifts are marked by a circle.

Supplement – Fig. S5

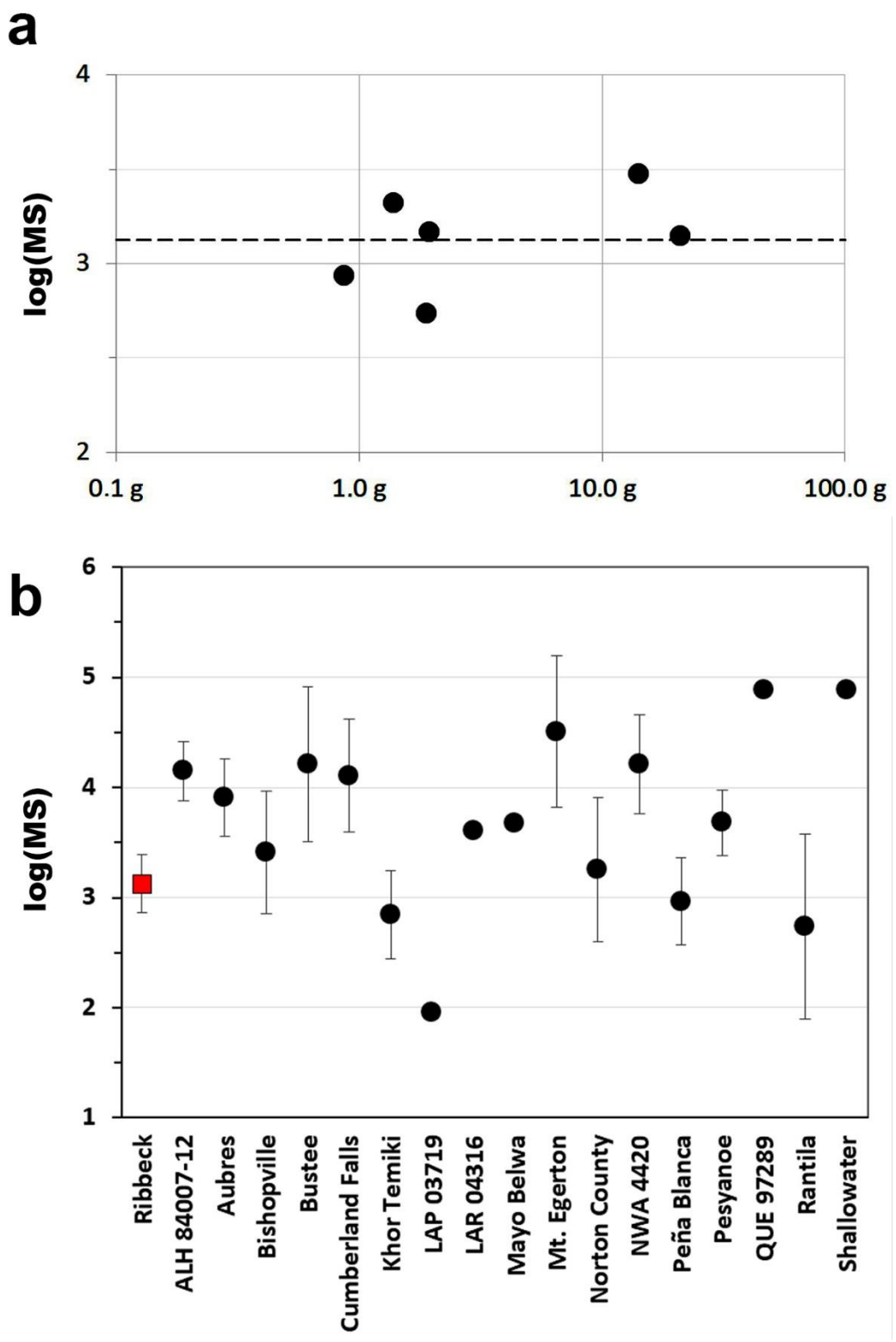

Fig. S5: (a) Magnetic susceptibility (MS) of six Ribbeck stones. (b) Magnetic susceptibility of the mean Ribbeck value (red square) compared to other members of the aubrite family (black points, taken from Rochette et al. (2009), partly expanded by own measurements). Error bars indicate standard deviations.

Supplement – Fig. S6

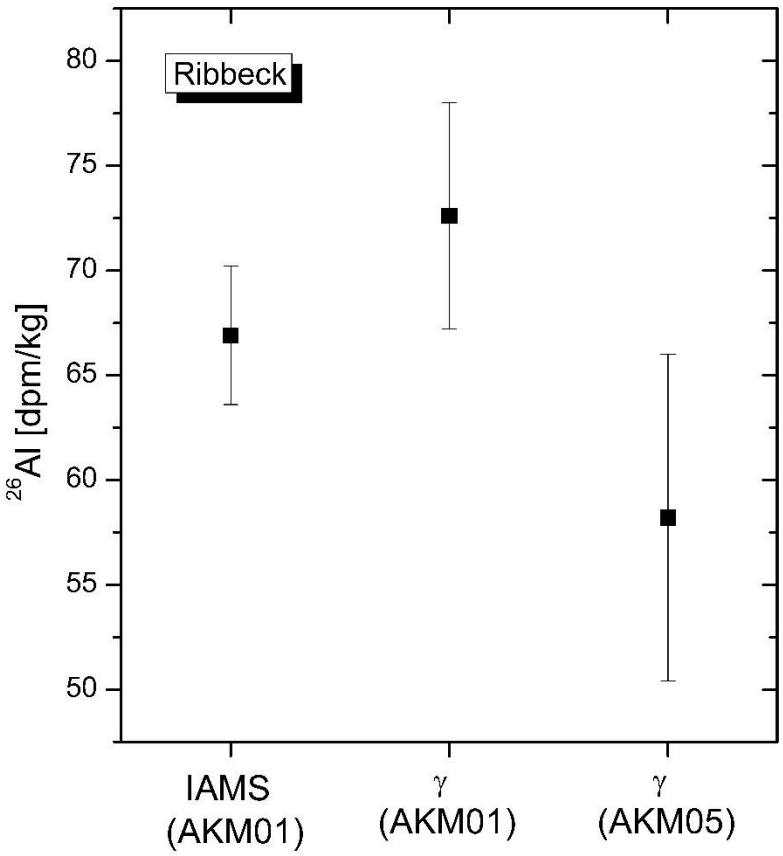

Fig. S6: The ^{26}Al value from instrumental accelerator mass spectrometry (IAMS; originating from a 0.75 g aliquot of AKM01) is in excellent agreement with the ^{26}Al values from gamma spectrometry (originating from AKM01 and AKM05).

Supplement – Fig. S7

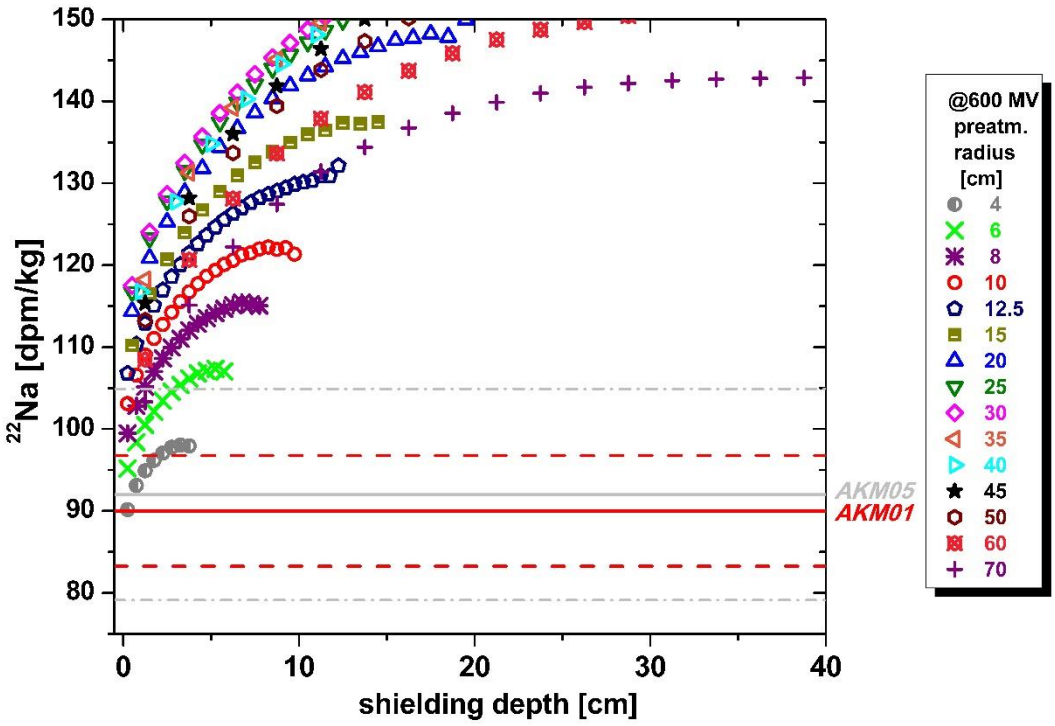

Fig. S7: Specific ^{22}Na activity measured in Ribbeck for AKM01 (red line with associated 1-sigma uncertainties) and AKM05 (gray line with associated 1-sigma uncertainties) by γ spectrometry compared to radius- and depth-dependent (saturation) production rate for ^{22}Na for L chondrites (Leya et al., 2021). The production rates of ^{22}Na are adapted to the chemical composition from Table 4 and are a function of the solar modulation that changes over short cycles of 11 years, hence data shown is for a mean value of 600 MV. The actual galactic cosmic ray fluxes for Ribbeck were slightly higher but as of yet have an unknown quantitative influence on the production rates (Leya, priv.com., 2023).

Supplement S2: Analytical Procedures

Mineralogical studies

An Axiophot polarizing microscope (Fa. ZEISS) was used for optical microscopy in transmitted and reflected light at the Institut für Planetologie (University of Münster). At the same institution, the brecciated texture of the Ribbeck sample was resolved with a JEOL 6610-LV electron microscope (SEM) and different mineral phases could be identified. Some chemical data were obtained using the INCA analytical program provided by Oxford Instruments for energy dispersive spectrometry (EDS).

By far, most quantitative mineral analyses from the Ribbeck aubrite breccia were obtained with a JEOL JXA 8530F electron microprobe (EPMA) at the Institut für Mineralogie (University of Münster), which was operated at 15 kV and a probe current of 15 nA. Synthetic and natural standards were used for wavelength dispersive spectrometry (WDS). As standards for mineral analyses, we used jadeite (Na), San Carlos olivine (Mg), kyanite (Al), hypersthene (Si), fluorite (F), fayalite (Fe), apatite (P), sanidine (K), chromium oxide (Cr), diopside (Ca), rhodonite (Mn), rutile (Ti), celestine (S), Co-metal (Co), and nickel oxide (Ni). The bulk Si, Fe, and Na concentrations (Table 4) are given by the mean concentrations of about 700 randomly obtained microprobe analyses on the Ribbeck thin section PL24001 (grid analysis). These results were also used to determine the modal composition of the 4.3 g aliquot of the Ribbeck sample AKM01 corrected after the procedure of van der Plas and Tobi (1965).

Bulk chemical analysis by ICP-SFMS and ICP-AES

A 155 mg sample from the crushed and homogenized material from the 4.3 g specimen (AKM01; Fig. 2, Table S1) was used for bulk chemical analyses at the University of Brest. The chemical bulk composition of Ribbeck was obtained using inductively coupled plasma atomic emission spectrometry (ICP-AES) and inductively coupled plasma sector field mass spectrometry (ICP-SFMS). The concentration reproducibility is generally greater than 5 %. Barrat et al. (2012, 2016) report further details concerning the analytical method.

Oxygen isotope analyses

For Ribbeck, the compositions of two chips (weighing 2.15 and 2.174 mg, respectively) removed from the ~4.3 g piece (AKM01; Fig. 2, Table S1) were obtained by means of laser fluorination in combination with a gas source mass spectrometer at the University of Göttingen.

The analytical techniques are given in detail in Pack and Herwartz (2014), Herwartz et al. (2014), Pack et al. (2016, 2017), and Peters et al. (2020). The $\delta^{17}O$ and $\delta^{18}O$ values are reported on the VSMOW (Vienna Standard Mean Ocean Water) scale, and the $\Delta'^{17}O$ is defined here as:

$$\Delta'^{17}O = 1000\ ln\left(\frac{\delta^{17}O}{1000} + 1\right) - 0.528 * 1000\ ln\left(\frac{\delta^{18}O}{1000} + 1\right)$$

We used a $\Delta'^{17}O$ value for San Carlos olivine of –0.052‰ to anchor $\delta^{17}O$ on the VSMOW scale, (average value of Pack et al. (2016), Sharp et al. (2016), and Wostbrock et al. (2020)). For the obtained data, the estimated measurement uncertainties are ±0.1‰ for $\delta^{18}O$ and ±0.01‰ for $\Delta'^{17}O$, and are also based on replicate analyses of the San Carlos olivine standard (1 SD).

Fourier transform infrared (FTIR) spectroscopy

Analysis in of the mid-infrared reflectance of the Ribbeck meteorite were performed at Institut für Planetologie at Universität Münster, Germany. For the infrared measurements we used a Bruker Vertex 70v equipped with a varying angle unit for bidirectional measurements and a liquid nitrogen-cooled MCT detector for analyzing the wavelength range between 6 µm and 18 µm. The sample compartment was evacuated to ~2 hPa and at room temperature (~21°C). For calibration, a commercial rough gold coted standard Infragold™ was used. We placed 0.04 g of the powdered sample in an alumina cup with a diameter of 1 cm and a depth of 0.5 mm and flattened it with a spatula, resulting in a mean bulk porosity of 0.68 assuming a raw grain density for aubrites of 3.2 g/cm^3 (Macke et al., 2011). 512 scans were accumulated for each measurement of background and sample. The spectrum was labeled with an identification number (ID 660) under which the spectrum can be found in the MERTIS IRIS Infrared database (http://bc-mertis-pi.uni-muenster.de).

Raman spectroscopy

Raman spectra were obtained at room conditions using a high-resolution confocal LabRam HR 800 spectrometer (Jobin–Yvon®) at the Institut für Mineralogie (University of Münster, Germany). Spectra were taken with a laser excitation wavelength of 532 nm using an 100 × objective resulting in a ~2 µm spot size on the sample. The spectral resolution is about 4 cm^{-1}. Our Raman measurements were carried out in the Stokes range from 200 cm^{-1} to 1200 cm^{-1} for feldspar and from 200 cm^{-1} to 700 cm^{-1}/900 cm^{-1} for the sulfides on a polished thin section. A calcite was used for the Stoke shift verification.

Titanium isotope analyses

For nucleosynthetic Ti isotope analyses of the Ribbeck meteorite, 48.9 mg of material from the homogenized powder of 0.75 g of the 4.3 g specimen (AKM01; Fig. 2, Table S1) was used. The powder was dissolved in octagonal Savillex® vials following the procedure in Bischoff et al. (2019). As described in Williams et al. (2021), Ti was separated and purified in a three-step anion exchange chromatography procedure. The blank of the full chemical procedure was 2 ng Ti, corresponding to a blank contribution of maximum 0.007 %. Following the description in Rüfenacht et al. (2023), the Ti isotope analyses were performed on a Thermo Scientific Neptune Plus multicollector inductively coupled plasma mass spectrometer (MC-ICPMS) at ETH Zurich). The measurements were done in high mass resolution (HR) with a mass resolving power R ~8000 [R = m/ ($m_{0.95}$-$m_{0.05}$)]. One single measurement consumed ~0.6 µg Ti and achieved a signal of ~40 V over a 10^{11} Ohm resistor on ^{48}Ti. Using the exponential law, the isotope values were corrected for instrumental mass bias by normalizing to the ^{49}Ti/^{47}Ti ratio of 0.749766 (Niederer et al., 1985). The data are reported relative to an in-house Alfa Aesar Ti wire standard in the ε-notation and applying the sample-standard bracketing method:

$$\varepsilon^{i}Ti = \left(\frac{^{i/47}Ti_{sample}}{^{i/47}Ti_{standard}} - 1 \right) x\ 10^{4},$$

where i stands for the isotope masses ^{46}Ti, ^{48}Ti, and ^{50}Ti. The isotope data were collected on two different days and include 10 measurement repetitions for Ribbeck. Parallel to the Ribbeck meteorite, the terrestrial rock standard BHVO-2 and the ordinary chondrite (OC) Forest Vale (H4) were measured to assess the accuracy and reproducibility of the measurements.

Non-contact profilometry

The surface height data of a freshly broken surface of the Ribbeck meteorite sample was imaged by a non-contact (light section method) optical profilometer (Keyence VR-6200) at 40x magnification with a pixel xy resolution of ~7 µm. The resulting raw digital terrain model (DTM) was detrended by fitting a plane through a set of uniformly distributed points selected on the raw DTM. The surface average slope and the Hapke mean slope are (mathematically described in as described in detail in section 2.3 of Marshal et al. (2024) then calculated onto the detrended DTM.

Instrumental accelerator mass spectrometry for cosmogenic ^{26}Al and ^{41}Ca

Accelerator mass spectrometry (AMS) has been used to detect long-lived cosmogenic radionuclides such as ^{26}Al and ^{41}Ca ($t_{1/2}$ = 0.705 and 0.104 Myr, respectively; Norris et al., 1983; Paul et al., 1991). A unique development at the Vienna Environmental Research Accelerator (VERA), an ion-laser interaction mass spectrometry (ILIAMS) system allows the isobar suppression by up to 14 orders of magnitude (Martschini et al., 2022). Thus, ILIAMS-assisted AMS, so-called instrumental AMS (IAMS), allows now the direct detection of ^{26}Al/^{27}Al ($\sim10^{-10}$) and ^{41}Ca/^{40}Ca ($\sim10^{-13}$) in crushed Ribbeck containing ~1 % intrinsic Al and Ca. Isobars from the natively abundant elements (20 % Mg, 1.2 ‰ K) do not cause any analysis problem, making radiochemical separation redundant. IAMS was performed on a crushed aliquot (~60 mg) of the homogenized powder of 0.75 g of the AKM01 specimen. For AlO^- extraction and ^{26}Al/^{27}Al measurements (Lachner et al., 2021) a small portion of the fine-grained powder was pressed in Cu cathodes without any metal binder. For ^{41}Ca/^{40}Ca 1.4 mg powder was mixed with ~12 mg of PbF_2 to increase CaF_3^- extraction from the Cs ion sputter source and finally also pressed in Cu cathodes. In-house standards Dhurmsala (^{26}Al/^{27}Al = (1.287±0.034) × 10^{-10}) and SMD-Ca-11 (^{41}Ca/^{40}Ca = (0.9944±0.0092) × 10^{-11}), traceable to primary standards (Rugel et al., 2016), were used for normalization. The total uncertainties of IAMS data include counting statistics and scatter for each sample, the variability of the measurements of the standards and the uncertainty of the nominal value of the standard material. For the conversion of the nuclide ratios into specific activities in disintegrations per minute (dpm) per kg, the Al and Ca concentrations of Table 4 (1.22 % Al; 1.20 % Ca) were used. These specific activities measured by IAMS are compared with Monte Carlo-calculation based chemistry, radius- and depth-dependent production rates (Leya and Masarik, 2009; Leya et al., 2021). The theoretical production rates are based in general on ordinary chondrite parameters (both matrix and actual sample), and we adjusted the sample chemistry to the bulk composition of Ribbeck, i.e., values from Table 4 plus calculated values for oxygen (46.1 %; based on the model abundance of 76 vol% enstatite, 15 vol% albite, and 5.5 vol% forsterite (see main text)) and sulfur (1.08 %; based on estimated 3 vol% sulfides). Oxygen, carbon (0.3‰) and nitrogen (0.031‰) (Grady et al., 1986) do not produce any ^{26}Al or ^{41}Ca, but in this way, all input elements add up to ~98 %. Similarly, theoretical production rates for ^{22}Na, originally developed for L chondrites, have been calculated (Leya et al., 2021). We are fully aware of the systematic errors, e.g., due to density differences and the matrix-dependent build up of secondary protons and neutrons, in applying ordinary chondrite calculations to an aubrite. We use the noble gas CRE ages to adopt

that both ^{26}Al and ^{41}Ca are in saturation, which was expected as aubrites have generally long CRE ages, i.e., >10 Ma peaking at 50 Ma (Keil 2010).

Noble gas mass spectrometry

An aliquot of 13.822±0.027 mg taken from 0.75 g of homogenized bulk powder of the 4.3 g fragment was analyzed for all stable noble gas isotopes of He-Xe using the in-house-built noble gas mass spectrometer "Albatros" at ETH Zurich (for technical details see Riebe et al., 2017). The sample, wrapped in Al foil, was heated to 110 °C in ultra-high vacuum for several days prior to analysis, to remove possibly adsorbed atmospheric gases. Gas extraction was performed in one step by fusion in a Mo-crucible heated at ~1700 °C. Blank corrections were <0.2% of the signals for all He and Ne isotopes, <11% for all Ar isotopes, but ~50% and ~60% for ^{84}Kr and ^{132}Xe, respectively. With Kr and Xe in the 1700 °C step being already small, total gas extraction was confirmed with other, more suitable samples in the same run.

Cosmogenic components

Since the data shows no evidence for a trapped (tr) Ne component, He and Ne (Table 6) are adopted as purely cosmogenic (cos), with additions of radiogenic (rad) $^{4}He_{rad}$ (Table 6). The measured $^{36}Ar/^{38}Ar$ ratio (3.63±0.04; Table 6) significantly differs from pure cosmogenic composition, indicating the presence of resolvable Ar_{tr} in addition to Ar_{cos} and $^{40}Ar_{rad}$. To determine $^{38}Ar_{cos}$ (Table 6), we performed a two-component deconvolution between $(^{36}Ar/^{38}Ar)_{cos}$ = 0.566-0.579 (derived with the model and the bulk chemical composition of Ribbeck) and $(^{36}Ar/^{38}Ar)_{tr}$ =5.32-5.34 (covering Q and air composition; Busemann et al., 2000; Nier, 1950).

Production rates and cosmic ray exposure (CRE) ages

We applied the ordinary chondrite (OC) matrix model by Leya and Masarik (2009), complemented with the bulk chemical composition of Ribbeck (Table 4) and the measured (= cos) $^{22}Ne/^{21}Ne$ ratio as shielding indicator (Table 6), to calculate the production rates of cosmogenic ^{3}He, ^{21}Ne, and ^{38}Ar and the respective cosmic ray exposure (CRE) ages (Table 6). Note that not only the chemical composition of the sample and its shielding conditions, but also the composition of the surrounding matrix controls the cosmogenic nuclide production.

Amongst the different meteorite matrices considered by Leya and Masarik (2009), an OC matrix is most appropriate to represent aubrites. However, differences in OC and aubrite matrix composition may influence the determination of production rates. Without additional constraints, we obtained possible preatmospheric meteoroid radii of 20 to 120 cm by comparing the measured $^{22}Ne/^{21}Ne$ with the model predictions (minor, randomly distributed individual matches between measured and modelled data, typically at unreasonably large sample depths >115 cm, were not considered). Based on the estimated preatmospheric meteoroid mass of 140 kg (Spurný et al., 2024) and a density for Ribbeck of ~2.6 g/cm^3 (Table 7) resulting in a preatmospheric spherical meteoroid radius of ~23 cm, we conservatively set the maximum radius in the model to 30 cm, allowing for a deviation from this estimated preatmospheric mass of ~50%.

U/Th-He and K-Ar gas retention ages

We determined radiogenic gas retention ages with the U/Th-He and K-Ar chronometers based on radiogenic ^4He and ^{40}Ar (Table 6) and the U, Th, and K concentrations in Ribbeck (Table 4). We used the measured (= cos) ^3He concentration and $(^4He/^3He)_{cos}$ = 5.2-6.1 (Wieler, 2002) to determine the concentration of $^4He_{rad}$ ($^4He_{tr}$ is negligible). To determine the $^{40}Ar_{rad}$ concentration, we calculated $^{40}Ar_{tr}$ based on $^{36}Ar_{tr}$ (see section "cosmogenic components") and $(^{40}Ar/^{36}Ar)_{tr}$ = 0-295.5 (conservatively covering Q, with no $^{40}Ar_{tr}$, and air composition; Busemann et al., 2000; Steiger and Jäger, 1977).

Radionuclide analyses by gamma spectrometry

Previous investigations showed that the activity level of meteorites lies for the most part in the order of or well below 1 Bq kg^{-1} (e.g., Povinec et al., 2015; Rosen et al., 2020; Bischoff et al., 2021). This requires for gamma spectrometric analyses the use of special, low-level gamma spectrometers at well-shielded locations. For this reason, the two Ribbeck samples AKM01B (19.55 g) and AKM05 (25.48 g) were measured non-destructively in the underground laboratory Felsenkeller (Niese et al., 1998) of the VKTA Rossendorf (Dresden). Contributions from the muonic part of the cosmic radiation are reduced there in total by a factor of 30-40 (Ludwig et al., 2019). The two gamma spectrometers used are situated in accessible shielding chambers and contain special shieldings made from selected, low-radioactivity materials. Both spectrometers are based on coaxial p-type high-purity germanium (HPGe) detectors with

enhanced front-side sensitivity for low-energy gamma rays and have relative efficiencies of 95 % and 92 %, respectively. The structure of both shieldings is graded: 10 and 5 cm, respectively, of electrolytic copper, 10 / 5 cm of low-activity lead (<3 Bq kg^{-1} ^{210}Pb) and 10 cm of standard lead (6 / 33 Bq kg^{-1} ^{210}Pb) (Neumaier et al., 2009; Köhler et al., 2009).

Spectrum acquisition started on January 29 (AKM01) and January 31 (AKM05), 2024, and was finished on February 26, 2024, after 28 and 26 days of measurement, respectively. Short breaks on the order of a few hours were necessary for spectrometer maintenance. All gamma spectrometric results are corrected for the decay between the moment of fall (January 21, 2024 1:32) and start of measurement and for the decay during measurement. The energy-dependent efficiency of the detectors was determined by the measurement of models of the pieces made of a material with known contents of natural radionuclides.

The gamma spectra showed for both pieces from AKM01and AKM05 gamma lines from the decay chains of ^{238}U and ^{232}Th and from ^{40}K. Additionally, cosmogenic radionuclides with half-lives ranging from 53 days (^{7}Be) to 705 000 yrs (^{26}Al) were detected.

Computed Tomography and Density measurements

X-ray computed tomography of F07 was performed at the Luxembourg Institute of Science and Technology used a RX Solutions EasyTom 160 operated at 90 kV with a tube current of 130 µA (11.7 W). X-ray radiographies were taken through 360° and reconstructed with the X-Act software package, resulting in a voxel size of 27.2 µm. Segmenting to derive total volume and metal fractions was done in ImageJ2.

The Ribbeck meteorite samples F69 and F82 were scanned in a CoreTom CT scanner from Tescan at the Helmholtz-Institute Freiberg for Resource Technology. The scans were performed with 8.4 µm voxel size (F69) and 9.1 µm voxel size (F82) respectively. Both scans were performed with a maximum X-ray energy of 160 kV, with a power of 15 W and using one 0.2 mm thick steel filter mounted at the source. The current used was optimized so that the resolution was limited by geometrical factors and not by the spot size of the beam. Reconstruction was done using Panthera 1.3.1. Image processing and visualization were done in Avizo 9.3.0. A 3D non-local-means filter (window = 10, neighbor = 3, similarity = 0.5) was used to remove noise with minimum impact on object boundaries.

In order to precisely determine the bulk volume of the meteorite samples, an optical 3D scan was carried out using the Zeiss GOM Atos Compact Scan. This scanner works with a structured-

light projector and a stereo camera setup. A blue light stripe pattern scans over the sample surface to identify the same sample spot in each detector pixel of the monochrome cameras after filtering. This is followed by triangulation and further processing.

The cameras and thus the measuring volume were adjusted to the size of the fragments at 170 x 130 x 115 mm³ in order to achieve a measuring point distance of 50 µm on the specimen. To prevent damage to the fragments, no scanning spray was used and no reference points were placed on the sample. The meteorite pieces were placed in their natural state on a turntable on which concentric reference points were attached to combine several scans. To compensate over- and under-exposure due to the different reflection of individual areas of the meteorite surface, different exposure times were chosen.

The specimens were scanned from two sides (top – bottom) from multiple perspectives. In the vertical direction shots were taken at different angle of incidence, starting from 90° (perpendicular to the turntable surface) in six steps of 15° up to a flat viewing angle of 15°. For each viewing angle, 12 images were then taken in horizontal rotation over the full 360° in 30° increments (see Figure below). The 72 individual shots of one side of the object were then stitched together into one view using the turntable's reference points.

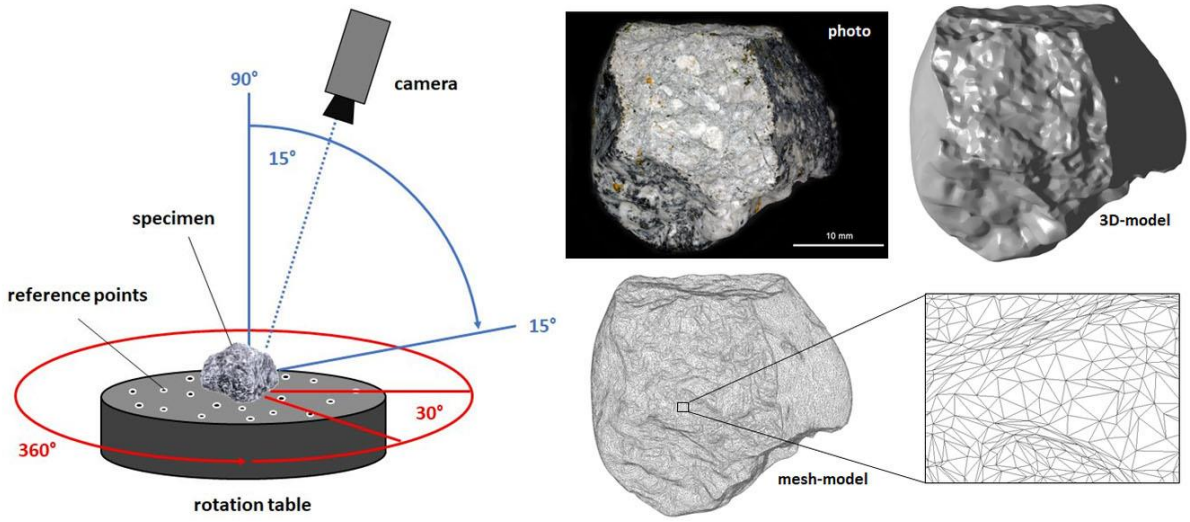

Schematic illustration of the GOM Atos Compact Scan fringe projection 3D-scanner and the use of the 3D mesh model

Since measurements were taken up to a very flat angle of inclination of 15°, the scan of the top and bottom side captured sufficient areas of the objects that are included in both views. This allows the two halves to be merged together exactly.

From the total of 144 individual images for each Ribbeck fragment, a 3D mesh model was created using polygonization, from which the volumes were determined. The 3D models also enable the 3D printing of casts of the meteorites.

Measurement of the grain density used a temperature-controlled Microtrac Belpycno L helium pycnometer operated with a 20 cm^3 reduction vessel at 20.0°C. An additional 10 cm^3 of calibrated aluminum filler disks provided a filling ratio of at least 50 vol%. The calibration of the vessel and filler volumes were checked against a crystal of synthetic CaF_2, which resulted in a difference of 0.05 % between the measured and theoretically expected density. Replicate volume determinations of the Ribbeck sample F07 were done with 16 individual measurement cycles each. The relative standard uncertainty of both replicates was 0.04 %. The mass was determined by weighing on an Ohaus Explorer semi-microbalance. The relative standard uncertainty obtained from repeated weighing was 0.004 %, and, therefore, did not contribute considerably to the final uncertainty of the density determination.

References of supplement section "methods"

Barrat J.-A., Zanda B., Moynier F., Bollinger C., Liorzou C., and Bayron G. 2012. Geochemistry of CI chondrites: Major and trace elements, and Cu and Zn isotopes. *Geochimica et Cosmochimica Acta* 83: 79-92.

Barrat J.-A., Gillet P., Dauphas N., Bollinger C., Etoubleau J., Bischoff A., and Yamaguchi A. 2016. Evidence from Tm anomalies for non-CI refractory lithophile element proportions in terrestrial planets and achondrites. *Geochimica et Cosmochimica Acta* 176: 1-17.

Bischoff A., Barrat J.-A., Berndt J., Borovicka J., Burkhardt C., Busemann H., Hakenmüller J., Heinlein D., Hertzog J., Kaiser J., Maden C., Meier M. M. M., Morino P., Pack A., Patzek M., Reitze M. P., Rüfenacht M., Schmitt-Kopplin P., Schönbächler M., Spurný P., Weber I., Wimmer K. and Zikmund T. 2019. The Renchen L5-6 chondrite breccia – the first confirmed meteorite fall from Baden-Württemberg (Germany). *Geochemistry – Chemie der Erde* 79: 125525.

Bischoff A., Alexander C. M. O'D., Barrat J.-A., Burkhardt C., Busemann H., Degering D., Di Rocco T., Fischer M., Fockenberg T., Foustoukos D. I., Gattacceca J., Godinho J. R. A., Harries D., Heinlein D., Hellmann J. L., Hertkorn N., Holm A., Jull A. J. T., Kerraouch I., King A. J., Kleine T., Koll D., Lachner J., Ludwig T., Merchel S., Mertens C. A. K., Morino P., Neumann W., Pack A., Patzek M., Pavetich S., Reitze M. P., Rüfenacht M., Rugel G., Schmidt C., Schmitt-Kopplin P., Schönbächler M., Trieloff M., Wallner A., Wimmer K., and Wölfer E. 2021. The old, unique C1 chondrite Flensburg – Insight into the first processes of aqueous alteration, brecciation, and the diversity of water-bearing parent bodies and lithologies. *Geochimica et Cosmochimica Acta* 293: 142–186.

Busemann H., Baur H., and Wieler R. 2000. Primordial noble gases in "phase Q" in carbonaceous and ordinary chondrites studied by closed-system stepped etching. *Meteoritics & Planetary Science* 35: 949-973.

Grady M. M., Wright I. P., Carr L. P., and Pillinger C. T. 1986. Compositional differences in enstatite chondrites based on carbon and nitrogen stable isotope measurements. *Geochimica et Cosmochimica Acta* 50: 2799-2813,

Herwartz D., Pack A., Friedrichs B., and Bischoff A. 2014. Identification of the giant impactor Theia in lunar rocks. *Science* 344: 1146-1150.

Keil K. 2010. Enstatite achondrite meteorites (aubrites) and the histories of their asteroidal parent bodies. *Chemie der Erde* 70: 295–317.

Köhler M., Degering D., Laubenstein M., Quirin P., Lambert M.-O., Hult M., Arnold D., Neumaier S., and Reyss J.-L. 2009. A new low-level ɣ-ray spectrometry system for environmental radioactivity at the underground laboratory Felsenkeller. *Applied Radiation and Isotopes* 67: 736-740.

Lachner J., Martschini M., Kalb A., Kern M., Marchhart O., Plasser F., Priller A., Steier P., Wieser A., and Golser R. 2021. Highly sensitive ^{26}Al measurements by Ion-Laser-InterAction Mass Spectrometry. *International Journal of Mass Spectrometry* 465: 116576.

Leya I. and Masarik J. 2009. Cosmogenic nuclides in stony meteorites revisited. *Meteoritics & Planetary Science* 44: 1061–1086.

Leya I., Hirtz J., and David J.-C. 2021. Galactic cosmic rays, cosmic-ray variations, and cosmogenic Nuclides in meteorites, *The Astrophysical Journal* 910: 136.

Ludwig F., Wagner L., Al-Abdullah T., Barnaföldi G. G., Bemmerer D., Degering D., Schmidt K., Suranyi G., Szücs T., and Zuber K. 2019. The muon intensity in the Felsenkeller shallow underground laboratory. *Astroparticle Physics* 112: 24-34.

Macke R. J., Britt D. T. and Consolmagno G. J. 2011. Density, porosity, and magnetic susceptibility of achondritic meteorites. *Meteoritics & Planetary Science* 46: 311-326.

Marshal R. M., Patzek M., and Rüsch O. 2024. Characterization of the micrometer scale surface roughness of meteoritic samples. *Icarus* 412: 115984.

Martschini M., Lachner J., Hain K., Kern M., Marchhart O., Pitters J., Priller A., Steier P., Wiederin A., Wieser A., and Golser R. 2022. 5 years of ion-laser interaction mass spectrometry – status and prospects of isobar suppression in AMS by lasers. *Radiocarbon* 64: 555–568.

Neumaier S., Wojcik M., Dombrowski H. and Arnold D. 2009. Improvements of a low-level gamma-ray spectrometry system at the underground laboratory "UDO". *Applied Radiation and Isotopes* 67: 726-730.

Niederer F. R., Papanastassiou D. A., and Wasserburg G. J. 1985. Absolute isotopic abundances of Ti in meteorites. *Geochimica et Cosmochimica Acta* 49: 835-851.

Nier A. O. 1950. A redetermination of the relative abundances of the isotopes of carbon, nitrogen, oxygen, argon and potassium. *Phys. Rev.* 77: 789-793.

Niese S., Köhler M., and Gleisberg B. 1998. Low-level counting techniques in the underground laboratory “Felsenkeller” in Dresden. *Journal of Radioanalytical and Nuclear Chemistry* 233: 167-172.

Norris T. L., Gancarz A. J., Rokop D. J., and Thomas K. W. 1983. Half-life of ^{26}Al. *Proc. of the 14th Lunar and Planetary Science Conference, Journal of Geophysical Research Suppl.* 8: B331-B333.

Pack A. and Herwartz D. 2014. The triple oxygen isotope composition of the Earth mantle and understanding Δ^{17}O variations in terrestrial rocks and minerals. *Earth and Planetary Science Letters* 390: 138-145.

Pack A., Tanaka R., Hering M., Sengupta S., Peters S., and Nakamura E. 2016. The oxygen isotope composition of San Carlos olivine on VSMOW2-SLAP2 scale. *Rapid Communications in Mass Spectrometry* 30: 1495-1504.

Pack A., Höweling A., Hezel D. C., Stefanak M., Beck A. K., Peters S. T. M., Sengupta S., Herwartz D., and Folco L. 2017. Tracing the oxygen isotope composition of the upper Earth atmosphere using cosmic spherules. *Nature Communications* 8: 15702.

Paul M., Ahmad I., and Kutschera W. 1991. Half-life of ^{41}Ca. *Z. Phys. A - Hadrons and Nuclei* 340: 249-254.

Peters S. T. M., Alibabaie N., Pack A., McKibbin S. J., Raeisi D., Nayebi N., Torab F., Ireland T., and Lehmann B. 2020. Triple oxygen isotope variations in magnetite from iron-oxide deposits, central Iran, record magmatic fluid interaction with evaporite and carbonate host rocks. *Geology* 48: 211-215.

Povinec P. P., Masarik J., Sykora I., Kovacik A., Beno J., Meier M. M. M., Wieler R., Laubenstein M., and Porubcan P. 2015. Cosmogenic nuclides in the Košice meteorite: Experimental investigations and Monte Carlo simulations. *Meteoritics & Planetary Science* 50: 880–892.

Riebe M. E. I., Welten K. C., Meier M. M. M., Wieler R., Barth M. I. F., Ward D., Laubenstein M., Bischoff A., Caffee M. W., Nishiizumi K., and Busemann H. 2017. Cosmic-ray exposure ages of six chondritic Almahata Sitta fragments. *Meteoritics & Planetary Science* 52: 2353-2374.

Rochette P., Gattacceca J., Bourot-Denise M., Consolmagno G. J., Folco L., Kohout T., Pesonen L., and Sagnotti L. 2009. Magnetic classification of stony meteorites: 3. Achondrites. *Meteoritics & Planetary Science* 44: 405-428.

Rosen A. V., Hofmann B. A., von Sivers M., Schumann M. 2020. Radionuclide activities in recent chondrite falls determined by gamma-ray spectrometry: Implications for terrestrial age estimates. *Meteoritics & Planetary Science* 55: 149–163.

Rüfenacht M., Morino P., Lai Y.-J., Fehr M. A., Haba M. K., and Schönbächler M. 2023. Genetic relationships of solar system bodies based on their nucleosynthetic Ti isotope compositions and sub-structures of the solar protoplanetary disk. *Geochimica et Cosmochimica Acta* 355: 110-125.

Rugel G., Pavetich S., Akhmadaliev S., Enamorado Baez S. M., Scharf A., Ziegenrücker R., and Merchel S. 2016. The first four years of the AMS-facility DREAMS: Status and developments for more accurate radionuclide data. *Nucl. Instr. Meth. Phys. Res. B* 370: 94-100.

Sharp Z. D., Gibbons J. A., Atudorei V., Pack A., Sengupta S., Shock E. L., and Knauth L. P. 2016. A calibration of the triple oxygen isotope fractionation in the SiO_2–H_2O system and applications to natural samples. *Geochimica et Cosmochimica Acta* 186: 105-119.

Steiger R. H. and Jäger E. 1977. Subcommission on geochronology: Convention on the use of decay constants in geo- and cosmochronology. *Earth and Planetary Science Letters* 36: 359-362.

Van der Plas L. and Tobi A. C. 1965. A chart for judging the reliability of point counting results. *American Journal of Science* 263: 87–90.

Weber I., Morlok A., Grund T., Bauch K. E., Hiesinger H., Stojic A., Grumpe A., Wöhler C., Klemme S., Sohn M., Martin D. J. P., and Joy K. H. 2018. A mid-infrared reflectance database in preparation for space missions. *Lunar Planet. Sci. Conf.* 48: #1430.

Wieler R. 2002. Cosmic-ray-produced noble gases in meteorites. *Rev. Mineral. Geochem*. 47: 125-170.

Williams N. H., Fehr M. A., Parkinson I. J., Mandl M. B., and Schönbächler M. 2021. Titanium isotope fractionation in solar system materials. *Chemical Geology* 568: 120009.

Wostbrock J. A., Cano E. J., and Sharp Z. D. 2020. An internally consistent triple oxygen isotope calibration of standards for silicates, carbonates and air relative to VSMOW2 and SLAP2. *Chemical Geology* 533: 119432.